Journal of the Optical Society of America B

OPTICAL PHYSICS

Numerical modeling of the coupling efficiency of single quantum emitters in photonic-crystal waveguides

Alisa Javadi,* Sahand Mahmoodian, Immo Söllner, and Peter Lodahl

Niels Bohr Institute, University of Copenhagen, Blegdamsvej 17, DK-2100 Copenhagen, Denmark
Corresponding author: javadi@nbi.ku.dk

Planar photonic nanostructures have recently attracted a great deal of attention for quantum optics applications. In this paper, we carry out full 3D numerical simulations to fully account for all radiation channels and thereby quantify the coupling efficiency of a quantum emitter embedded in a photonic-crystal waveguide. We determine the leakage from the quantum emitter to the surrounding environment and study its spectral and spatial dependence. The spatial maps of the coupling efficiency, the β factor, reveal that even for moderately slow light, a near-unity β factor is achievable and is remarkably robust to the position of the emitter in the waveguide.   ©2018 Optical Society of America

1. INTRODUCTION

Enhancing the spontaneous emission rate of a quantum emitter by placing it in an optical cavity was first suggested by Purcell [1]. In the following decades, it was realized that the spontaneous emission rate of a quantum emitter can also be suppressed by placing it in a photonic bandgap [2–5]. This has led to a significant research effort to manipulate the photonic environment surrounding quantum emitters to suppress coupling to unwanted radiation modes and boost coupling to specific localized modes. The spontaneous emission rate of a quantum emitter scales with the projected local density of optical states (LDOS). Significant enhancement of spontaneous emission rates has been demonstrated in optical cavities [6,7], nanophotonic waveguides [8], and surface plasmon modes [9], while suppression of spontaneous emission has been measured in the bandgap region of a photonic crystal [10].

Recently, there has been a growing interest in quantum emitters coupled to planar nanostructures due to the potential of the platform to create high-efficiency light–matter interfaces. An efficient interface would have a wide range of applications, from building quantum networks [11] to efficient quantum computation [12,13]. Indeed, different quantum emitters such as quantum dots [14–18], diamond color centers [19,20], and atoms [21,22] have been efficiently coupled to planar nanostructures. Planar photonic crystals typically only possess a bandgap for a single polarization and for in-plane guided

propagation. Nevertheless, this partial bandgap can greatly reduce the LDOS for transition dipoles lying in the middle of the waveguide ($z = 0$ plane in the rest of the paper) by suppressing the coupling rate to the radiation modes, and therefore decrease the spontaneous emission rate of embedded quantum emitters [10,23]. By creating waveguides or cavities in the bandgap frequency range, the spontaneous emission can preferentially be directed with very high efficiency into a single mode. A combination of suppression of the coupling to the radiation modes and enhancement of coupling to a photonic-crystal waveguide (PCW) mode has been predicted to enable a deterministic single-photon source [24,25]. The fraction of emitted light that is coupled into the waveguide is defined as the β factor. The coupling of single quantum dots to PCWs has been studied by several groups [8,26–28], and a record value of $\beta > 98.4\%$ was recently achieved [29].

An important feature of PCWs is their wide bandwidth contrary to cavities. However, the β factor depends significantly on the spatial position of the emitter in the PCW due to the coupling to the waveguide mode as well as the coupling to radiation modes. The spatial and spectral dependencies of the coupling to the PCW guided mode are well understood [30], since they can be obtained from eigenfunctions computed using standard techniques, e.g., the plane-wave expansion method [30,31]. In contrast, the spatial and spectral dependencies of the unguided radiation continuum in PCWs have thus far only

been quantified at certain spatial positions [25,32]. A full mapping of the radiation modes is essential in order to find the β factor and thereby determine how large coupling efficiencies may be obtained under experimentally realistic conditions.

In order to accurately map out the position dependence of the β factor, we develop the necessary tools to carry out a detailed analysis of the LDOS in a PCW. The main challenge in modeling an infinite PCW in a finite computation domain is that, along the propagation direction, open boundary conditions are required. Although perfectly matched layers are typically good approximations for open boundaries, they fail in inhomogeneous dielectric structures [33], particularly at low group velocities. To overcome this problem, we derive Dirichlet boundary conditions, whose phase and amplitude match a propagating PCW mode excited by a dipole at an arbitrary point inside the waveguide. Armed with these boundary conditions, we compute the LDOS contribution from the radiation continuum for a range of frequencies across the waveguide band. We show that the coupling to the radiation continuum is highly suppressed in a PCW. We map out the dependence of the coupling to the radiation continuum on the position, frequency, and orientation of the dipole. The resulting β factor is remarkably robust to spatial position, dipole orientation, and spectral tuning of the emitter, a fact which has been confirmed experimentally [29].

This paper is arranged as follows: Section 2 discusses the different decay channels for an emitter embedded in a PCW and introduces the parameters that govern the emitter dynamics. Section 3 includes the details of the simulations. We present and discuss the results of the numerical simulations in Section 4. Section 5 sums up our results and gives an overview of various applications that could benefit from an efficient light–matter interface. The two appendices include the convergence tests, as well as a short overview of the decay dynamics of an emitter in a photonic crystal and comparison to a PCW.

2. ELECTRODYNAMICS OF A QUANTUM EMITTER IN A PCW

Figure 1(a) shows the band diagram of the transverse electric (TE) modes of a W1 PCW membrane [30]. Inside the
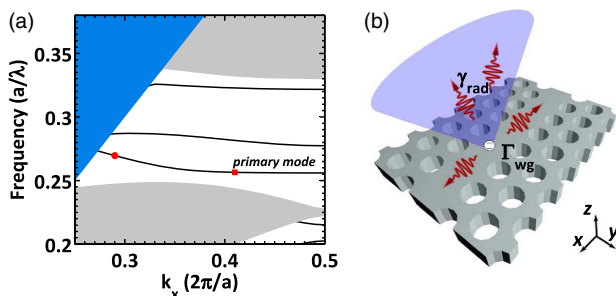

Fig. 1. (a) Band diagram of a PCW in a membrane for TE modes. The solid black lines are the guided modes of the waveguide. The gray regions mark the membrane guided modes. The blue region is the continuum of the radiation modes that are not bound to the membrane. The red circle and square mark the frequencies corresponding to $n_g = 5$ and $n_g = 58$, respectively. (b) Sketch of a quantum emitter in the middle of a PCW, showing the coupling to radiation continuum (γ_rad) and to the guided mode (γ_wg).

bandgap, light is mainly guided by three highly confined waveguide modes, and by matching the PCW to the targeted emitter, the emitter is typically coupled to a single propagating mode [cf. Fig. 1(a), solid black lines]. The waveguide modes are highly dispersive, and the group velocity of the mode is reduced as its frequency approaches the band edge, where the slow-down factor $n_g = \frac{c}{d\omega/dk}$ (also known as the group index) ideally diverges. Due to the partial bandgap of the 2D PCW membrane, there exists a continuum of modes that are not guided by the waveguide and leak to the surrounding environment [blue area in Fig. 1(a)]. In real PCWs, unavoidable fabrication imperfections influence light transport, leading to multiple scattering effects. As a consequence, the guided mode is coupled to radiation modes or back-scattered to the oppositely propagating mode in the waveguide [34–36], which has been quantitatively studied in Ref. [37]. Effects of disorder become dominating for long waveguides and large group indices, and may be eliminated by reducing both. In the present work we only consider PCWs where effects of disorder are negligible, which in practice means that we consider quantum emitters coupled only to moderately large values of $n_g = 100$. Such a slow-down factor is experimentally achievable [29].

An emitter embedded in a PCW can emit photons either to the guided modes of the PCW or to the radiation continuum, as schematically illustrated in Fig. 1(b). The general form for the spontaneous emission rate of an excited emitter with an arbitrarily oriented transition dipole moment $\boldsymbol{d}$ can be related to $\boldsymbol{d}$ and the projected LDOS as [14,38]

$$\gamma = \frac{\pi\omega}{\hbar\epsilon_0}|\boldsymbol{d}|^2\rho(\omega_0,\mathbf{r}_0,\mathbf{n_d}), \tag{1}$$

where

$$\rho(\omega_0,\mathbf{r}_0,\mathbf{n_d}) = \sum_{\mathbf{k}}|\mathbf{n_d}\cdot\mathbf{u}_{\mathbf{k}}^*(\mathbf{r}_0)|^2\delta(\omega_0-\omega_{\mathbf{k}}), \tag{2}$$

$\mathbf{n_d}$ is a complex vector with unit length oriented along the dipole moment, $\rho(\omega_0,\mathbf{r}_0,\mathbf{n_d})$ is the projected LDOS, $\mathbf{u}_{\mathbf{k}}$ denotes the electric field eigenmode, and $\int\epsilon(\mathbf{r})\mathbf{u}_{\mathbf{k}}(\mathbf{r})\cdot\mathbf{u}_{\mathbf{k}}^*(\mathbf{r})d^3r = 1$.

The modes in Fig. 1(a) are classified into three categories: the guided modes of the PCW, the slab guided modes present outside the bandgap region [gray region in Fig. 1(b)], and the continuum of radiation modes [39]. At each frequency, the total decay rate of the emitter can be written as a sum of the contribution from these three sets of modes in addition to any residual contributions from coupling to transverse magnetic (TM) modes, i.e., $\gamma_\mathrm{total}(\omega) = \gamma_\mathrm{wg}(\omega) + \gamma_\mathrm{rad}(\omega) + \gamma_\mathrm{slab}(\omega) + \gamma_\mathrm{TM}(\omega)$, where the explicit dependence on spatial position and dipole orientation has been omitted for brevity. The β factor quantifying the fraction of radiation coupled to the primary waveguide mode is defined as $\beta = \frac{\gamma_\mathrm{wg}}{\gamma_\mathrm{total}}$. Ideally, one is interested in coupling a quantum emitter to a single optical mode, as it allows the quantum emitter to be used for a wide range of applications [11,14], which requires suppressing the interaction between the quantum emitter and the unwanted optical modes. This can be done either by designing the nanostructure to spectrally detune the unwanted optical modes from the resonance of the quantum emitter, or by placing the quantum emitter in a node of the unwanted optical modes. In the case of the TM modes, this can be done by placing the

quantum emitter on the symmetry plane ($z = 0$) and making sure that the transition dipole moments are oriented along the symmetry plane. In this case, no coupling to TM modes would be present, i.e., $\gamma_{\text{TM}} = 0$. The frequency range of interest for a PCW single-photon source is mainly the primary guided mode in the bandgap region, where also $\gamma_{\text{slab}} = 0$.

The contribution to the β factor describing the coupling to the waveguide, γ_{wg}, is straightforwardly determined by computing the eigenvalue and the corresponding eigenvectors of the electric and magnetic fields $\mathbf{E}_{pg}(\omega, r)$, $\mathbf{H}_{pg}(\omega, r)$ [25,32,40,41]. The corresponding Purcell factor is defined as

$$F_p^{\text{wg}} = \frac{\gamma_{\text{wg}}}{\gamma_0} = \frac{6\pi^2 c^3 \epsilon_0 |\mathbf{E}_{\text{pg}} \cdot \mathbf{n}_{\mathbf{d}}^*|^2}{\omega^2 \int_{\text{unitcell}} d^3 r n \, \text{Re}[\mathbf{E}_{\text{pg}} \times \mathbf{H}_{\text{pg}}^*]/a}, \quad \textbf{(3)}$$

where n is the refractive index of the membrane material, a is the lattice constant of the PCW, and $\gamma_0 = \frac{n\omega^3 d^2}{3\pi\epsilon_0 \hbar c^3}$ is the decay rate of an emitter in a homogenous material of refractive index n.

3. COMPUTING THE COUPLING OF A DIPOLE TO THE RADIATION CONTINUUM

In this section, we detail how to extract the contribution of the coupling to the radiation continuum to the β factor, i.e., γ_{rad}, which is the most challenging part of the problem. This coupling is quantified by the Purcell factor of coupling to the radiation modes, which is denoted F_p^{rad}. It is given by $F_p^{\text{rad}} = \gamma^{\text{rad}}/\gamma_0 = P^{\text{rad}}/P_0$, where P_0 and P^{rad} are the power emitted from the dipole in the reference medium and the power emitted to the radiation modes in the nanophotonic structure, respectively. The total power emitted from the dipole can be extracted by integrating Poynting's vector over a closed surface around the dipole, i.e., $P_{\text{total}} = 1/2 \, \text{Re}[\oint d\mathbf{s} \cdot \mathbf{E} \times \mathbf{H}^*]$. The Purcell factor can thereby be determined.

A main consideration in numerical simulations of optical problems is to ensure proper convergence, i.e., the computed quantities must not depend on the physical size of the computational domain. At the same time, it is desirable to limit the geometrical size of the simulation domain as much as possible in order to make the simulation efficient. A general approach to tackling these problems has been to introduce an absorber in the boundaries of a finite simulation domain and adiabatically absorb the incoming wave [42,43]. This can be applied when the geometry of the computational domain is invariant in the direction perpendicular to the boundary and the solutions are propagating waves rather than evanescent fields. In the case of a PCW, the simulation domain is invariant at the z boundaries. Moreover, the waveguide mode has a very low intensity at the y boundaries and the simulation domain can be terminated using a homogenous domain. Hence, we can apply perfectly matched-layers (PMLs) at these boundaries. However, this is not applicable along the propagation direction (x) in the PCW. The generalization of PMLs to photonic-crystal waveguides is challenging [33], particularly for slowly propagating Bloch modes.

Instead of using PMLs along the direction of the waveguide (x), a better choice is to introduce Dirichlet boundary conditions for the purpose of mimicking an open system. This

corresponds to setting $E|_{x\pm} = C_\pm$ at the two ends of the waveguide ($x_\pm$), where $C_\pm$ is the Dirichlet boundary condition for the electric field. In general, $C_\pm$ has contributions both from the primary mode of the waveguide and the radiation modes, but the main contribution stems from the guided mode of the waveguides that are extended by many optical wavelengths, i.e., the contributions from radiation modes are negligible. This is checked explicitly by running a convergence test while varying the length of the simulation domain. Since the Purcell factor of the guided mode is known, one can quantify the power that the dipole radiates to the guided mode. With the knowledge of the Bloch wavevector of the guided mode, we can therefore determine both the phase and the magnitude of the guided mode at the edge of the computation domain for a given dipole. This determines the phase and amplitude of the Dirichlet boundary condition. The electric fields at the right and left boundaries (x_+ and x_-) can be written as

$$E|_{x\pm} = -|A_0^{r(l)}| e^{-i\phi(\mathbf{r}_0)} \mathbf{E}_{\text{pg}}^{(*)}(x_\pm) e^{\pm ikx_\pm}, \quad \textbf{(4)}$$

where $\mathbf{r}_0$ is the position of the dipole in the unit cell and $\phi(\mathbf{r}_0)$ is the phase of the projection of $\mathbf{E}_{\text{pg}}$ on the dipole at the position $\mathbf{r}_0$. The amplitudes $A_0^{r(l)}$ can be calculated from the knowledge of the guided modes of the PCW using the Green function formalism. For linear dipoles, these amplitudes simplify to

$$|A_0^r| = |A_0^l| = \sqrt{\frac{F_p^{\text{wg}} P_0}{1/a \int_{\text{unitcell}} d^3 r \, \text{Re}[\mathbf{E}_{\text{pg}}^* \times \mathbf{H}_{\text{pg}}]}},$$

$$\phi = \arg(-i\mathbf{E}_{\text{pg}}(\mathbf{r}_0) \cdot \mathbf{d}). \quad \textbf{(5)}$$

The term in the denominator is the average power in the cross section of the eigenmode. γ_{rad} can subsequently be calculated as the difference between γ_{wg} and γ_{total}. The particular form of the boundary conditions in Eq. (4) assures that both in-phase and out-of-phase reflections from the boundaries are suppressed. However, for a PCW typically $\gamma_{\text{rad}} \ll \gamma_{\text{wg}}$, and even small reflections and numerical inaccuracies in γ_{wg} or γ_{total} limit the obtainable precision of γ_{rad}. This can be circumvented by calculating γ_{rad} directly by integrating Poynting's vector over a sheet surrounding the dipole and leaving out the integration over the boundaries normal to the waveguide direction. This is indicated by the green box in Fig. 2, which illustrates the geometry of the computation domain. The sheet extends inside the membrane and the U-like shape of the sheet helps to reduce the simulation domain in the y direction. Due to the symmetry of the structure and the position of the dipole being in the center of the slab, the solutions of Maxwell's equations are eigenvectors of the mirror symmetry operator about the $z = 0$ plane. As a result, the simulation domain can be cut in half along this symmetry plane with the following boundary conditions: $E_z(z = 0) = 0$ and $\frac{\partial}{\partial z}\{E_x, E_y\}|_{z=0} = 0$. The PCW membrane has a length of $l = (2n + 1)a$ and a width of $w = \sqrt{3}(2m + 1)a$, and is surrounded by an air box of height D_z. The refractive index of the PCW slab is chosen to be 3.5, corresponding to the refractive index of GaAs. The simulation domain is encapsulated by PMLs on all sides (blue box in Fig. 2). The width of the PML layer is W_{PML}. Dirichlet boundary conditions override the PMLs on the two ends of
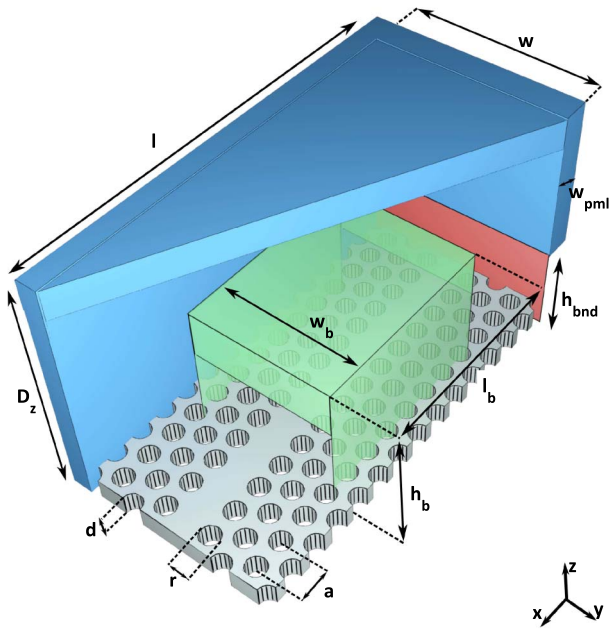
Fig. 2. A cut through the simulation domain. The blue box is the PML layer around the air domain. The green box is the integration surface that captures the radiation modes, and the red plane is where the Dirichlet boundary conditions are applied.

in a PCW with the correct boundary conditions. The total power emitted from the waveguide is calculated by integrating Poynting's vector over a small box around the current element. The coupling rate γ_{rad} is extracted by integrating Poynting's vector over the radiation box. We repeat all the simulations for $n_g = 5$, 20, 58, and 120. These correspond to realistic values of the slow-down factor of light, which have been obtained experimentally in GaAs PCWs [29,44].

We use the finite element package COMSOL to carry out the numerical simulations. We run these simulations on a Linux server with four CPUs, each with four cores (Xeon E5-2620) and 256 GB of random access memory. We use a mesh with tetrahedral elements of varying size to accurately map out the features of the PCW. The maximum distance between the mesh nodes in each of the simulation domains is $0.41a/n$, where n is the refractive index of the domain. The length of the simulation domain is $33a$ for the simulations reported in the rest of the paper, unless specified otherwise. For these parameters, the linear system of equations includes around 20 million degrees of freedom. It takes 1 h to solve for the electric field and LDOS for each dipole orientation, position, and frequency. We use the general residual method (GMRES) to diagonalize the resulting matrices, and multifrontal massively parallel solver (MUMPS) on a coarse mesh to obtain the precondition for the iterative solver.

simulation domain normal to the waveguide direction (red plane in Fig. 2). The heights of these planes are h_{bnd} and they cover the full waveguide in the y direction. The green box in Fig. 2 resembles the box that captures the radiation modes. l_b, w_b, and h_b are the length, width, and height of the radiation box. Note that Fig. 2 is not to scale.

We assume a PCW with periodicity $a = 240$ nm, hole radius $r = a/3$, and a membrane thickness of $d = \frac{2}{3}a$. The length of the simulation domain is $l = 33a$. Table 1 presents the rest of the parameter values that were used in the computations presented in the paper. We use a radiation box which is slightly smaller than the full simulation domain ($l_b \sim 0.94l$) in order to avoid direct scattering from the boundaries to the radiation box. To establish these numbers we have carried out rigorous convergence tests. Appendix A contains the results of some of the convergence tests for the most sensitive parameters, l, l_{bnd}, and h_b. From the convergence test results, we estimate that the values of γ_{rad} are accurate to within 5%.

The simulation procedure can be summarized as follows: We first carry out an eigenvalue calculation to determine the eigenfrequency, group index n_g, eigenvector of the primary guided mode, and F_p^{wg} for a given dipole position. Using Eq. (4), we determine the correct amplitudes for the respective boundaries of the waveguide. We use a small linear current element oscillating at frequency ω as a current source and run a finite element frequency domain simulation of a dipole

4. RESULTS

The Purcell factor of a quantum emitter coupled to a waveguide is an important figure of merit, determining the rate of photon generation and the ability to overcome decoherence processes. We first use the frequency domain eigenvalue calculations to reproduce the very well-known results for F_p^{wg}, Purcell factor due to coupling to the waveguide mode [32]. Figure 3 shows the position and frequency dependence of F_p^{wg} for x- and y-oriented dipoles within a unit cell of the waveguide. The four columns correspond to dipoles at different frequencies $n_g = 5$, 20, 58, and 120, respectively. The Purcell factor is less than 1 at $n_g = 5$, but it scales linearly with the group index and reaches 23 at $n_g = 120$. These results compare very well to the previous reports [32,35]. At the band edge of the waveguide, the group index and consequently the Purcell factor diverge. However, in practice this Van Hove singularity in the LDOS is damped by Anderson localization of light induced by unavoidable fabrication disorder [45].

The actual excitation of the waveguide mode by a dipole emitter is shown in Fig. 4, which plots $|\mathbf{E}|$ for a y-oriented dipole in the antinode of the E_y field for $n_g = 5$ and $n_g = 58$, corresponding to fast and slow light propagation in the PCW. The plots are zoom-ins around the position of the dipole, and it should be mentioned that the color bars have been saturated since $|\mathbf{E}|$ diverges at the position of the point source. Furthermore, a "chevron feature" in the field profile is observed around the dipole, which is a manifestation of dipole-induced light localization coming from the coupling to evanescent modes of the PCW [2,46–49]. We also observe that the Dirichlet boundary conditions suppress the reflections from the boundaries of the simulation domain very effectively, i.e., the field intensities on the right-hand and left-hand sides of the
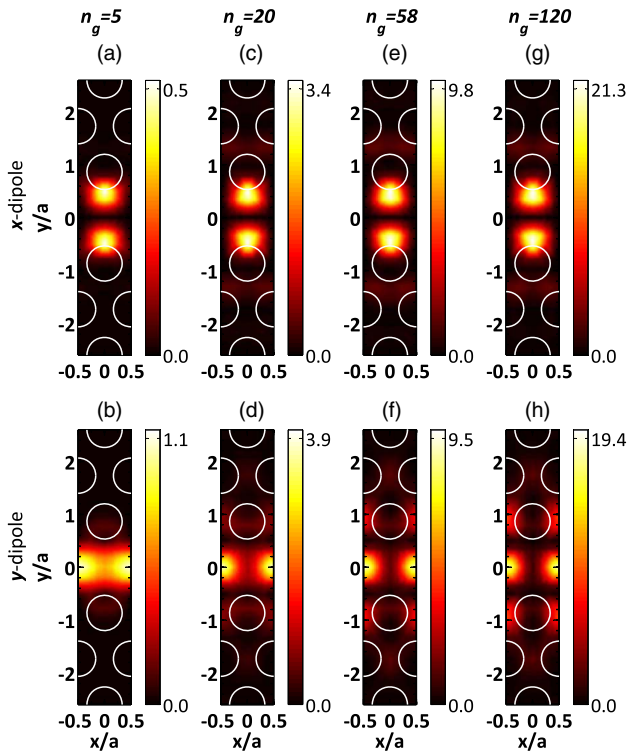
Table 1. Parameter List

Parameter	w	D_z	l_b	w_b	h_b	h_{bnd}
Value	$9\sqrt{3}a$	$6.6a$	$31a$	$8\sqrt{3}a$	$2.5a$	$2a$

Fig. 3. Spatial map of the waveguide Purcell factor, F_p^{wg}, for x- and y-dipole orientations (upper and lower row, respectively) and for modes with different group indices: (a) and (b) $n_g = 5$; (c) and (d) $n_g = 20$; (e) and (f) $n_g = 58$; and (g) and (h) $n_g = 120$. The white circles represent the air holes. The light–matter interaction is enhanced as the light propagation slows down, and hence the maximum value of F_p^{wg} increases. The spatial dependence of F_p^{wg} follows the Bloch mode of the PCW.
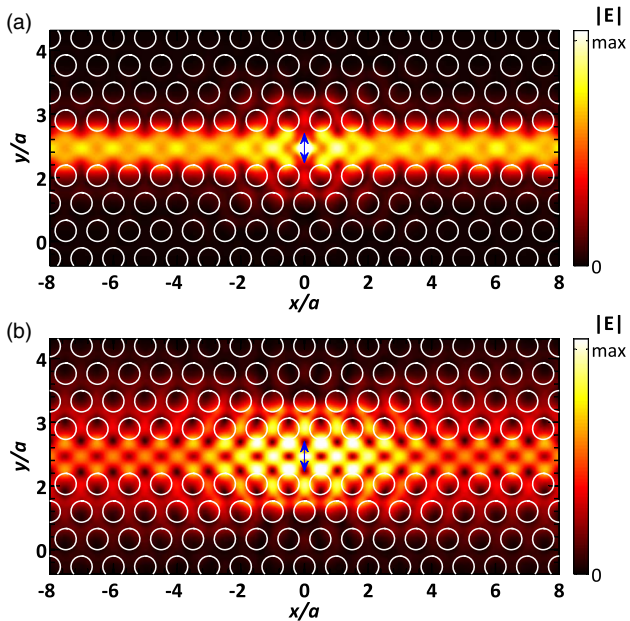

Fig. 4. Spatial map of the magnitude of the electric field generated by a y-dipole placed in the antinode of E_y for (a) $n_g = 5$ and (b) $n_g = 58$. The blue arrow shows the dipole and its orientation. The color scale is saturated at the point of the dipole.

simulation domain are uniform (within $\approx 7\%$), as expected from an infinite system. The field profiles plotted in Fig. 4 are subsequently integrated, as detailed in the previous section, in order to extract coupling to radiation modes.

Subsequently we discuss the results of the computations of the coupling to radiation modes. Figure 5 shows the position dependence of the Purcell factor associated with the coupling to radiation continuum, $F_p^{\text{rad}} = \gamma_{\text{rad}}/\gamma_0$, inside one unit cell. These results have been reconstructed by placing a dipole at different positions in the PCW, extracting F_p^{rad} as described in Section 3 for each position, and then interpolating the results to create Fig. 5. We find that the suppression is better than a factor of 10 for most spatial positions in Fig. 5, and importantly F_p^{rad} has a complex spatial structure. On the contrary, the frequency dependence of F_p^{rad} is rather weak and, e.g., changes only about 10% for a y-oriented dipole between $n_g = 5$ and $n_g = 120$. The smallest achievable Purcell factor is $F_p^{\text{rad}} = 0.005$, i.e., suppression of radiation modes by a factor of 200 relative to the emission rate of the dipole in a homogeneous medium. The strong suppression of radiation modes in 2D photonic-crystal membranes was first predicted in Ref. [23] for photonic crystals without defects. Interestingly, the suppression achieved in a PCW reaches the value obtainable in a photonic crystal without defects, demonstrating that the missing row of holes in the PCW does not induce additional leakage
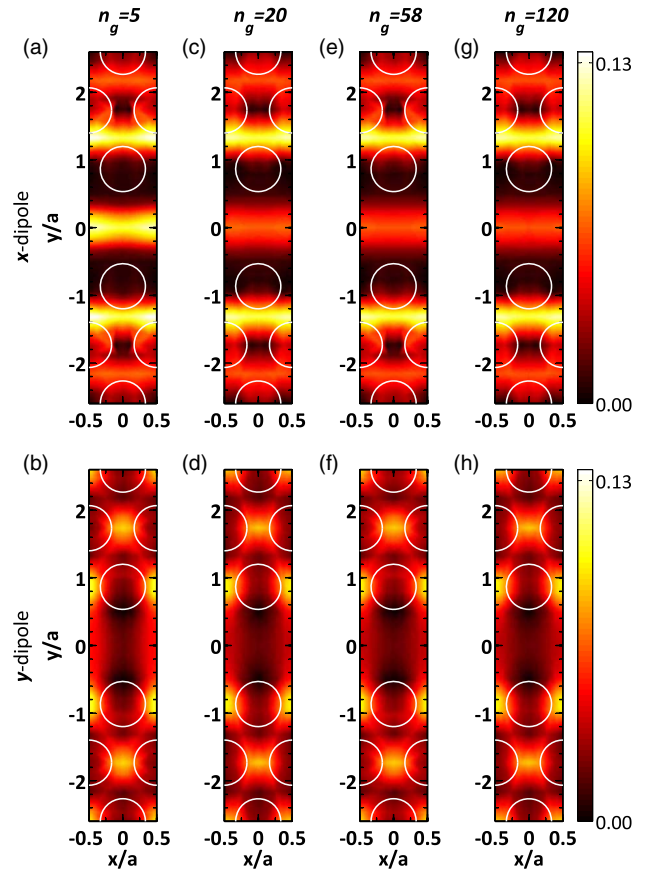

Fig. 5. Map of the coupling to the radiation modes as quantified by F_p^{rad} for x- and y-dipole orientations: (a) and (b) at $n_g = 5$; (c) and (d) at $n_g = 20$; (e) and (f) at $n_g = 58$; and (g) and (h) at $n_g = 120$. We find $F_p^{\text{rad}} \leq 0.13$ for all positions and a minimum value of $F_p^{\text{rad}} = 0.005$.

of the light from the membrane; see Appendix B for further details.

Finally, the spatial map of the β factor and its frequency dependence is investigated (see Fig. 6). Here, the green and the blue contours correspond to $\beta = 0.80$ and $\beta = 0.96$, respectively. Note that the implemented color bar showing the magnitude of the β factor is highly nonlinear. Even at low n_g, cf. Figs. 6(a) and 6(b), a large β factor can be achieved (higher than 96%) although limited to relatively small spatial regions in the PCW. Increasing n_g by moving into the slow-light region [cf. Figs. 6(c)–6(h)] increases β factor significantly, and we find $\beta \geq 0.96$ for a very wide range of dipole positions. More quantitatively, for any dipole located within $\pm a$ from the center of the waveguide, $\beta \geq 0.96$ at the experimentally achievable value of $n_g = 58$. This demonstrates the remarkable robustness of the β factor towards spatial and spectral detuning, which was already confirmed experimentally where the statistics of the β factor of more than 70 different quantum dots in a PCW were reported [29]. It is also worth mentioning that it takes between 55 and 60 h of computation time to produce one of the panels in Fig. 6.

Disorder in the position and shape of the air holes affects the performance of photonic-crystal nanostructures [36,50]. In the context of the classical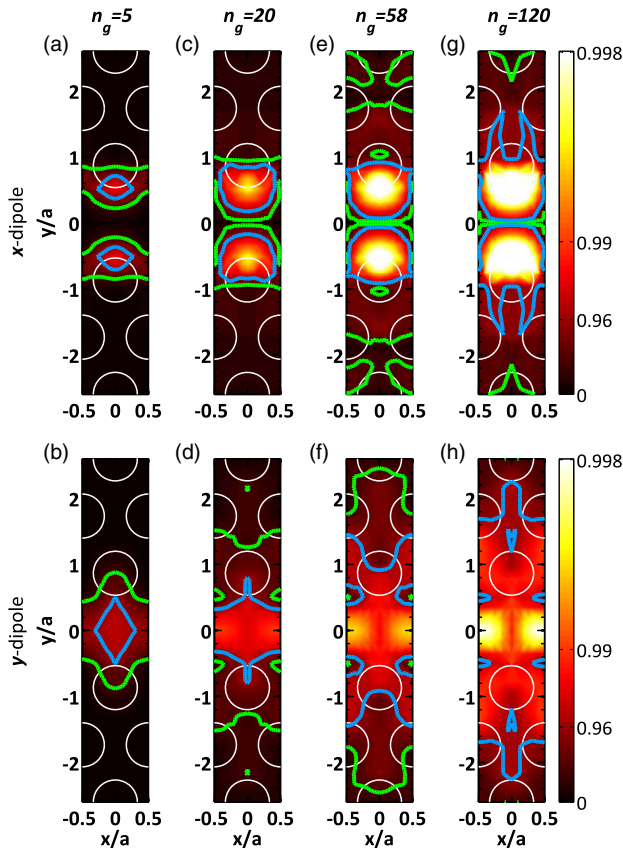 light transport, it is well established that disorder can induce out-of-plane losses, backscattering, and localization [34–36,45,50–53]. Around the band edge of the waveguide, and typically within 3–4 nm from the band edge, a series of Anderson localized modes limit useful bandwidth of the waveguide. In the context of light–matter interaction, the disorder-localized modes can inhibit or enhance the interaction between the quantum emitter and the disorder localized mode [54,55], which is more relevant close to the band edge, as disorder-induced localization is most significant in this region. Moreover, disorder can break the symmetry of the structure in the z direction and hence mix the TE and TM modes, which can result in coupling between the quantum emitter and the TM modes. However, away from the band edge, these fluctuations are unlikely to affect the β factor significantly. A recent experimental study already confirmed strongly suppressed coupling of quantum emitters to the radiation modes [10] in the presence of typical amounts of fabrication disorder. Appendix B shows the numerically expected Purcell factor of coupling to the radiation modes for ideal dipoles positioned in the bandgap of a perfect photonic crystal. The results reported in Ref. [10] are comparable to the numerically expected values, and hence indicate that the typical amounts of disorder that are encountered in the state-of-the-art nanofabrication methods are not detrimental for achieving high coupling efficiency between the waveguide mode and the embedded quantum emitters. A more quantitative conclusion would require numerical modeling of dynamics of emitters in the presence of disorder, which is outside the scope of this paper.

5. CONCLUSIONS

We have presented detailed numerical calculations of the β factor in a PCW. A key step has been to adopt mixed boundary conditions, i.e., Dirichlet boundary conditions at the terminations of the waveguide and PMLs at the other boundaries to treat the radiation modes. Based on this approach, we calculated the coupling rate from a quantum emitter to different optical channels in a PCW. We achieve an accuracy of better than 1% of the estimation of the β factor. Thanks to the speed of our numerical method, we accurately mapped out the position dependence of the β factor which had been missing so far. Our results show that the coupling from the emitter to the radiation continuum is highly suppressed compared to an emitter in a homogenous medium. The spatial dependence of γ_{rad} quantifies that a suppression factor larger than 10 is achieved for most regions in the PCW and for all frequencies of the waveguide band. As a direct consequence, the β factor is close to unity for essentially all emitter locations in the PCW, even for moderately slow light propagation. The detailed simulations confirm the remarkable robustness of the β factor against spatial position and frequency of the quantum emitter. Such a high coupling efficiency is of importance for a wide range of photonic quantum technology applications, including on-demand single-photon sources, multi-qubit gates [56], and single-photon transistors [57,58].

Fig. 6. Map of the β factor for x- and y-oriented dipoles: (a) and (b) at $n_g = 5$; (c) and (d) at $n_g = 20$; (e) and (f) at $n_g = 58$; and (g) and (h) at $n_g = 120$. The green and blue contours correspond to $\beta = 0.8$ and $\beta = 0.96$, respectively. Note that the highly nonlinear scale bar (i.e., β) is close to unity in very large spatial ranges.

APPENDIX A: INFLUENCE OF THE SIMULATION PARAMETERS ON γ_{rad}

Figure 7 presents some of the convergence tests carried out to ensure the validity of the simulations and to justify the choice of

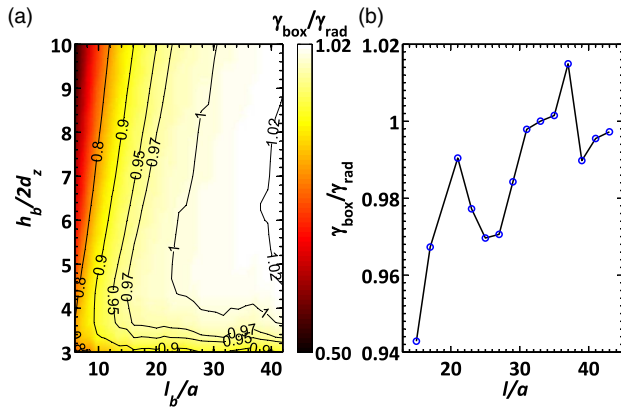**Fig. 7.** Dependence of γ_{box} on the size of the integration box. For $l_b/a > 25$ and $h_b/2d_z > 4$, γ_{box} fluctuates by less than 5%. (b) Dependence of γ_{box} on the actual size of the simulation domain. Both (a) and (b) are calculated for y-oriented dipoles in the anti-node of the E_y field. The frequency of the dipole corresponds to $n_g = 58$.

the radiation box size. We choose $\gamma_{box}/\gamma_{rad}$ as the target parameter for the convergence tests, where γ_{box} is the amount of radiation captured by the radiation box of size h_b and l_b, and γ_{rad} is the value reported in Fig. 5. From Fig. 7(a), we conclude that for $l_b/a > 25$ and $h_b/2d_z > 4$, the value of γ_{box} is independent of the size of the box to within 5%. Furthermore, the convergence of γ_{rad} with the size of the actual simulation domain is plotted in Fig. 7(b), displaying a similar precision. These convergence tests were carried out for a y-oriented dipole at the E_y antinode and with $n_g = 58$. We repeated the same tests for dipoles at a few more positions, orientations, and frequencies with very similar results.

APPENDIX B: POSITION AND FREQUENCY DEPENDENCE OF COUPLING TO RADIATION MODES IN A PHOTONIC CRYSTAL

As a comparison, we present the position and frequency dependence of F_p^{rad} for dipoles located in a photonic-crystal membrane without any waveguide defect region. These simulations were carried out in a similar fashion as for the PCW case, but they did not require Dirichlet boundary conditions as the photonic crystal already suppresses the light propagation, and hence PML boundary conditions are adequate. Figure 8 maps out the position-dependence of F_p^{rad} inside the bandgap of a photonic crystal for two orthogonal dipole orientations. Furthermore, the frequency dependence of F_p^{rad} for an emitter in the photonic crystal is displayed. The bandgap of the photonic crystal extends from $a/\lambda = 0.256$ to $a/\lambda = 0.360$. The main feature is the inhibition of spontaneous emission inside the bandgap of the photonic crystal, which reaches values as high as 168. These values are very similar to what is found in PCWs (see Fig. 5), and hence we conclude that the missing row of holes in the PCW does not significantly alter the coupling to the radiation modes. We note that these results compare very well to the values reported in Ref. [23].
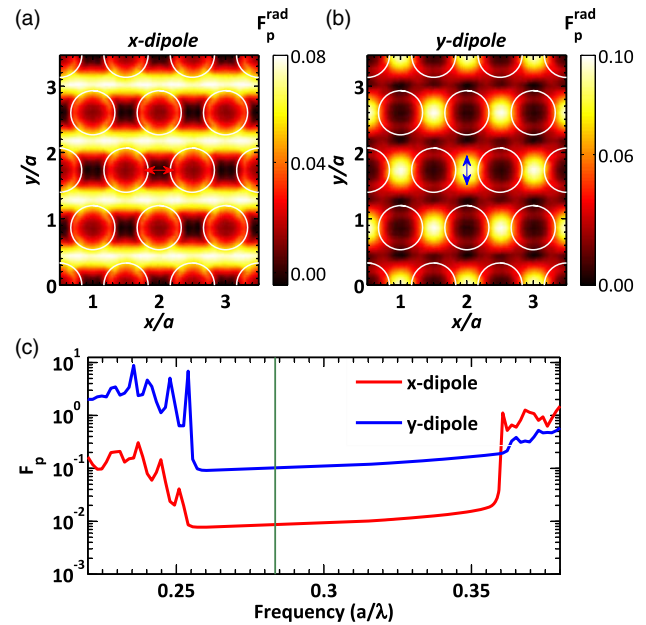

Fig. 8. (a) and (b) Spatial dependence of F_p^{rad} for x- and y-oriented dipoles inside the bandgap of a photonic crystal membrane. The maximum of F_p^{rad} is ~1/10 and its minimum value is ~1/168. The frequency of the emitter corresponds to the vertical green line in (c). (c) Frequency dependence of F_p^{rad} for the two dipole positions and orientations shown in (a) and (b).

REFERENCES

1. E. M. Purcell, "Spontaneous emission probabilities at radio frequencies," Phys. Rev. **69**, 681 (1946).
2. V. P. Bykov, "Spontaneous emission from a medium with a band spectrum," Sov. J. Quantum Electron. **4**, 861–871 (1975).
3. E. Yablonovitch, "Inhibited spontaneous emission in solid-state physics and electronics," Phys. Rev. Lett. **58**, 2059–2062 (1987).
4. P. Lodahl, A. F. van Driel, I. S. Nikolaev, A. Irman, K. Overgaag, D. Vanmaekelbergh, and W. L. Vos, "Controlling the dynamics of spontaneous emission from quantum dots by photonic crystals," Nature **430**, 654–657 (2004).
5. M. Fujita, S. Takahashi, Y. Tanaka, T. Asano, and S. Noda, "Simultaneous inhibition and redistribution of spontaneous light emission in photonic crystals," Science **308**, 1296–1298 (2005).
6. J. M. Gérard, B. Sermage, B. Gayral, B. Legrand, E. Costard, and V. Thierry-Mieg, "Enhanced spontaneous emission by quantum boxes in a monolithic optical microcavity," Phys. Rev. Lett. **81**, 1110–1113 (1998).
7. D. Englund, D. Fattal, E. Waks, G. Solomon, B. Zhang, T. Nakaoka, Y. Arakawa, Y. Yamamoto, and J. Vučković, "Controlling the spontaneous emission rate of single quantum dots in a two-dimensional photonic crystal," Phys. Rev. Lett. **95**, 013904 (2005).
8. T. Lund-Hansen, S. Stobbe, B. Julsgaard, H. Thyrrestrup, T. Sünner, M. Kamp, A. Forchel, and P. Lodahl, "Experimental realization of highly efficient broadband coupling of single quantum dots

to a photonic crystal waveguide," Phys. Rev. Lett. **101**, 113903 (2008).

9. A. V. Akimov, A. Mukherjee, C. L. Yu, D. E. Chang, A. S. Zibrov, P. R. Hemmer, H. Park, and M. D. Lukin, "Generation of single optical plasmons in metallic nanowires coupled to quantum dots," Nature **450**, 402–406 (2007).

10. Q. Wang, S. Stobbe, and P. Lodahl, "Mapping the local density of optical states of a photonic crystal with single quantum dots," Phys. Rev. Lett. **107**, 167404 (2011).

11. H. J. Kimble, "The quantum internet," Nature **453**, 1023–1030 (2008).

12. V. Paulisch, H. Kimble, and A. González-Tudela, "Universal quantum computation in waveguide QED using decoherence free subspaces," New J. Phys. **18**, 043041 (2016).

13. I. M. Mirza and J. C. Schotland, "Two-photon entanglement in multiqubit bidirectional-waveguide QED," Phys. Rev. A **94**, 012309 (2016).

14. P. Lodahl, S. Mahmoodian, and S. Stobbe, "Interfacing single photons and single quantum dots with photonic nanostructures," Rev. Mod. Phys. **87**, 347–400 (2015).

15. A. Javadi, I. Söllner, M. Arcari, S. L. Hansen, L. Midolo, S. Mahmoodian, G. Kiršanskė, T. Pregnolato, E. Lee, J. Song, S. Stobbe, and P. Lodahl, "Single-photon non-linear optics with a quantum dot in a waveguide," Nat. Commun. **6**, 8655 (2015).

16. D. Pinotsi, P. Fallahi, J. Miguel-Sanchez, and A. Imamoglu, "Resonant spectroscopy on charge tunable quantum dots in photonic crystal structures," IEEE J. Quantum Electron. **47**, 1371–1374 (2011).

17. S. G. Carter, T. M. Sweeney, M. Kim, C. S. Kim, D. Solenov, S. E. Economou, T. L. Reinecke, L. Yang, A. S. Bracker, and D. Gammon, "Quantum control of a spin qubit coupled to a photonic crystal cavity," Nat. Photonics **7**, 329–334 (2013).

18. M. N. Makhonin, J. E. Dixon, R. J. Coles, B. Royall, I. J. Luxmoore, E. Clarke, M. Hugues, M. S. Skolnick, and A. M. Fox, "Waveguide coupled resonance fluorescence from on-chip quantum emitter," Nano Lett. **14**, 6997–7002 (2014).

19. M. Lončar and A. Faraon, "Quantum photonic networks in diamond," MRS Bull. **38**(2), 144–148 (2013).

20. A. Sipahigil, R. E. Evans, D. D. Sukachev, M. J. Burek, J. Borregaard, M. K. Bhaskar, C. T. Nguyen, J. L. Pacheco, H. A. Atikian, C. Meuwly, R. M. Camacho, F. Jelezko, E. Bielejec, H. Park, M. Lončar, and M. D. Lukin, "An integrated diamond nanophotonics platform for quantum-optical networks," Science **354**, 847–850 (2016).

21. T. Tiecke, J. Thompson, N. de Leon, L. Liu, V. Vuletić, and M. Lukin, "Nanophotonic quantum phase switch with a single atom," Nature **508**, 241–244 (2014).

22. A. Goban, C.-L. Hung, S.-P. Yu, J. D. Hood, J. A. Muniz, J. H. Lee, M. J. Martin, A. C. McClung, K. S. Choi, D. E. Chang, O. Painter, and H. J. Kimble, "Atom-light interactions in photonic crystals," Nat. Commun. **5**, 3808 (2014).

23. A. F. Koenderink, M. Kafesaki, C. M. Soukoulis, and V. Sandoghdar, "Spontaneous emission rates of dipoles in photonic crystal membranes," J. Opt. Soc. Am. B **23**, 1196–1206 (2006).

24. V. S. C. Manga Rao and S. Hughes, "Single quantum dot spontaneous emission in a finite-size photonic crystal waveguide: proposal for an efficient on chip single photon gun," Phys. Rev. Lett. **99**, 193901 (2007).

25. G. Lecamp, P. Lalanne, and J. P. Hugonin, "Very large spontaneous-emission β Factors in photonic-crystal waveguides," Phys. Rev. Lett. **99**, 023902 (2007).

26. S. J. Dewhurst, D. Granados, D. J. P. Ellis, A. J. Bennett, R. B. Patel, I. Farrer, D. Anderson, G. A. C. Jones, D. A. Ritchie, and A. J. Shields, "Slow-light-enhanced single quantum dot emission in a unidirectional photonic crystal waveguide," Appl. Phys. Lett. **96**, 031109 (2010).

27. T. B. Hoang, J. Beetz, L. Midolo, M. Skacel, M. Lermer, M. Kamp, S. Höfling, L. Balet, N. Chauvin, and A. Fiore, "Enhanced spontaneous emission from quantum dots in short photonic crystal waveguides," Appl. Phys. Lett. **100**, 061122 (2014).

28. A. Laucht, S. Pütz, T. Günthner, N. Hauke, R. Saive, S. Frédérick, M. Bichler, M.-C. Amann, A. Holleitner, M. Kaniber, and J. J. Finley,

"A waveguide-coupled on-chip single-photon source," Phys. Rev. X **2**, 011014 (2012).

29. M. Arcari, I. Söllner, A. Javadi, S. Lindskov Hansen, S. Mahmoodian, J. Liu, H. Thyrrestrup, E. H. Lee, J. D. Song, S. Stobbe, and P. Lodahl, "Near-unity coupling efficiency of a quantum emitter to a photonic crystal waveguide," Phys. Rev. Lett. **113**, 093603 (2014).

30. J. D. Joannopoulos, S. G. Johnson, J. N. Winn, and R. D. Meade, *Photonic Crystals: Molding the Flow of Light* (Princeton University, 2008).

31. S. G. Johnson and J. D. Joannopoulos, "Bloch-iterative frequency-domain methods for Maxwell's equations in a planewave basis," Opt. Express **8**, 173–190 (2001).

32. V. S. C. Manga Rao and S. Hughes, "Single quantum-dot Purcell factor and β-factor in a photonic crystal waveguide," Phys. Rev. B **75**, 205437 (2007).

33. A. F. Oskooi, L. Zhang, Y. Avniel, and S. G. Johnson, "The failure of perfectly matched layers, and towards their redemption by adiabatic absorbers," Opt. Express **16**, 11376–11392 (2008).

34. S. Hughes, L. Ramunno, J. F. Young, and J. E. Sipe, "Extrinsic optical scattering loss in photonic crystal waveguides: role of fabrication disorder and photon group velocity," Phys. Rev. Lett. **94**, 033903 (2005).

35. S. Mazoyer, J. P. Hugonin, and P. Lalanne, "Disorder-induced multiple scattering in photonic-crystal waveguides," Phys. Rev. Lett. **103**, 063903 (2009).

36. V. Savona, "Electromagnetic modes of a disordered photonic crystal," Phys. Rev. B **83**, 085301 (2011).

37. S. Smolka, H. Thyrrestrup, L. Sapienza, T. B. Lehmann, K. R. Rix, L. S. Froufe-Pérez, P. D. García, and P. Lodahl, "Probing statistical properties of Anderson localization with quantum emitters," New J. Phys. **13**, 063044 (2011).

38. L. Novotny and B. Hecht, *Principles of Nano-Optics* (Cambridge University, 2007).

39. S. G. Johnson, P. R. Villeneuve, S. Fan, and J. D. Joannopoulos, "Linear waveguides in photonic-crystal slabs," Phys. Rev. B **62**, 8212–8222 (2000).

40. J. R. de Lasson, T. Christensen, J. Mørk, and N. Gregersen, "Modeling of cavities using the analytic modal method and an open geometry formalism," J. Opt. Soc. Am. A **29**, 1237–1246 (2012).

41. Y. Chen, T. R. Nielsen, N. Gregersen, P. Lodahl, and J. Mørk, "Finite-element modeling of spontaneous emission of a quantum emitter at nanoscale proximity to plasmonic waveguides," Phys. Rev. B **81**, 125431 (2010).

42. J.-P. Berenger, "A perfectly matched layer for the absorption of electromagnetic waves," J. Comp. Phys. **114**, 185–200 (1994).

43. W. C. Chew and W. H. Weedon, "A 3D perfectly matched medium from modified Maxwell's equations with stretched coordinates," Microwave Opt. Technol. Lett. **7**, 599–604 (1994).

44. N. A. Wasley, I. Luxmoore, R. Coles, E. Clarke, A. Fox, and M. Skolnick, "Disorder-limited photon propagation and Anderson-localization in photonic crystal waveguides," Appl. Phys. Lett. **101**, 051116 (2012).

45. P. D. Garca, A. Javadi, H. Thyrrestrup, and P. Lodahl, "Quantifying the intrinsic amount of fabrication disorder in photonic-crystal waveguides from optical far-field intensity measurements," Appl. Phys. Lett. **102**, 031101 (2013).

46. S. John and J. Wang, "Quantum optics of localized light in a photonic band gap," Phys. Rev. B **43**, 12772–12789 (1991).

47. J. S. Douglas, H. Habibian, C.-L. Hung, A. Gorshkov, H. J. Kimble, and D. E. Chang, "Quantum many-body models with cold atoms coupled to photonic crystals," Nat. Photonics **9**, 326–331 (2015).

48. E. Munro, L. C. Kwek, and D. E. Chang, "Optical properties of an atomic ensemble coupled to a band edge of a photonic crystal waveguide," New J. Phys. **19**, 083018 (2017).

49. G. Calajó, F. Ciccarello, D. Chang, and P. Rabl, "Atom-field dressed states in slow-light waveguide qed," Phys. Rev. A **93**, 033833 (2016).

50. J. Topolancik, B. Ilic, and F. Vollmer, "Experimental observation of strong photon localization in disordered photonic crystal waveguides," Phys. Rev. Lett. **99**, 253901 (2007).

51. D. Gerace and L. C. Andreani, "Disorder-induced losses in photonic crystal waveguides with line defects," Opt. Lett. **29**, 1897–1899 (2004).

52. N. Mann, A. Javadi, P. Garca, P. Lodahl, and S. Hughes, "Theory and experiments of disorder-induced resonance shifts and mode-edge broadening in deliberately disordered photonic crystal waveguides," Phys. Rev. A **92**, 023849 (2015).

53. P. D. Garca, G. Kiršanskė, A. Javadi, S. Stobbe, and P. Lodahl, "Two mechanisms of disorder-induced localization in photonic-crystal waveguides," Phys. Rev. B **96**, 144201 (2017).

54. L. Sapienza, H. Thyrrestrup, S. Stobbe, P. D. Garca, S. Smolka, and P. Lodahl, "Cavity quantum electrodynamics with Anderson localized modes," Science **327**, 1352–1355 (2010).

55. A. Javadi, S. Maibom, L. Sapienza, H. Thyrrestrup, P. D. García, and P. Lodahl, "Statistical measurements of quantum emitters coupled to Anderson-localized modes in disordered photonic-crystal waveguides," Opt. Express **22**, 30992–31001 (2014).

56. S. Mahmoodian, P. Lodahl, and A. S. Sørensen, "Quantum networks with chiral-light-matter interaction in waveguides," Phys. Rev. Lett. **117**, 240501 (2016).

57. D. E. Chang, A. S. Sørensen, E. A. Demler, and M. D. Lukin, "A single-photon transistor using nanoscale surface plasmons," Nat. Phys. **3**, 807–812 (2007).

58. D. Witthaut, M. D. Lukin, and A. S. Sørensen, "Photon sorters and QND detectors using single photon emitters," Europhys. Lett. **97**, 50007 (2012).